

A FE Based Global-Submodel Simulation Approach for Shape Compensation and Predicting Failure in Metal Parts Fabricated by Laser Powder Bed Fusion

Kaushik Das, Hongqing Sun, Geng Yun, Enqiang Lin, Reza Yavari, Anton Salem, Syed Zia Uddin, Nicholas Lajoie, Jack Jenny, Joseph Petsinger

VulcanForms, 112 Barnum Road,
Devens, MA 01434

Abstract

We use a two-stage workflow for print simulation. Stage 1 is a fast global pass. It runs layer by layer on a voxel mesh. We use either full thermo-mechanical physics or an inherent-strain surrogate, both with elastic behavior. The model predicts a distortion field. We project that field onto the part's triangulated surface to create a compensated geometry. We refine the mesh where distortion changes quickly. We leave top skins and other visually important faces unchanged to preserve appearance. Stage 2 focuses on local detail. We build compact submodels only in high-strain regions found in Stage 1. These submodels use conformal hexahedral meshes. They include elastic-plastic material laws and a ductile-failure rule that depends on stress triaxiality. Displacements from the global run are applied as boundary conditions. This keeps the models small but still accurate for local stress-strain. We also monitor strain where supports meet the part. That helps us choose scan and support strategies so parts stay strong during printing but break away cleanly afterward. This approach reproduces defects such as warping, thermal buckling, and shrink lines. It agrees well with measurements of distortion, failure locations, and layer temperatures.

Introduction

Laser powder bed fusion (LPBF) is an additive manufacturing process that uses a high-powered laser to selectively melt and fuse successive layers of metal powder, creating intricate components layer by layer. This technique excels at producing near net shape parts with complex geometries, lightweight designs, and high-performance mechanical properties, while significantly reducing material waste compared to traditional manufacturing methods.

LPBF faces challenges of thermal-induced distortion and cracking during part fabrication, which can cause parts to be dimensionally out of specification. Table 1 lists some of the causes of dimensional errors of printed parts. So carefully designed supports must be used to effectively manage heat distribution, reduce distortion, and maintain structural stability during the fabrication process. In addition, stock material is often added to the outer surfaces of the printed part, followed by subtractive machining to remove the excess and achieve dimensional accuracy, but this approach can be complex, as support may be difficult to remove and can leave residual stress or surface blemishes.

Table 1: Causes of geometric nonconformance between printed and target geometry

Causes	Magnitude of deviation (μm)
CAD file to STL/3MF format conversion	< 10
Geometric error during slicing	< 10
Layer height; staircase surface	Depends on layer height. Usually, 25-50.
End and start melt-pool shape at the boundary	It depends on scanning strategy. Usually 0 – 50.
Melt-pool width on the boundary	It depends on scanning strategy. Usually, 0 – 100.
Dross formation and overhang surface roughness	It depends on scanning strategy. Usually, 0-100
Laser trajectory error, part curvature resolution	It depends on scanning strategy. Usually, 75-100.
Machine imperfection/drift of laser trajectory	It depends on scanning strategy. Usually, 0-50.
Uncontrolled cooling down of part and plate due to print pauses	It depends on material and part size. Usually, 10-200.
Thermal shrinkage and residual stress induced distortion	It depends on material and part size. Can be between 10 – 2000 or larger for large parts.
Build plate distortion due to residual stress in the parts printing on top of it (plate and part layout)	It depends on material, part size and plate’s structural and thermal boundary conditions. Can be between 10 – 2000 or larger for large parts.
High temperature creep during VSR	It depends on material and part size.
Residual stress induced during rapid cooling during VSR due to spatial temperature gradient and/or due to mismatched thermal coefficient of expansion between the part and the plate material	It depends on the material of the part and the plate and their sizes.
Spring back deformation during to EDM/part-plate separation (if a VSR step was not performed)	It depends on the material of the part and its size.
High temperature (creep during) HIP	It depends on the material of the part and its size
Print to print and printer to printer variation	-
Measurement uncertainty	It depends on the measurement method. Can be in the order of 0 - 50
Surface erosion during bead blasting, chemical etching etc.*	It depends on the process. Can be in the order of 0 - 50

To address these challenges that arise from thermal shrinkage and residual stress build up during the print process, numerical simulation, notably using the finite element method (FEM), plays a crucial role in predicting and mitigating distortion, thereby guiding manufacturing processes to reduce risks [1, 2, 3, 4, 5, 6, 7]. Various numerical methods are employed, such as multi-scale FEM, the inherent strain method (ISM) [8, 9, 10, 11], and the thermal circuit network (TCN) [12]. The ISM, for instance, offers a rapid approach for predicting residual stresses and distortions across an entire component, typically requiring mechanical simulation and calibration steps. Distortion compensation strategies involve utilizing predicted distortion data, often derived from FEM simulations, to pre-distort the original Computer Aided Design (CAD) model in the inverse direction. The goal is to produce a modified design that, when printed, will result in a final component with significantly reduced distortion¹. Experimental validation is critical for confirming the accuracy of these predictive models, employing techniques like 3D optical scanning (e.g., GOM scanning) for distortion measurement, and Electronic Speckle Pattern Interferometry (ESPI) and the Contour Method for residual stress measurement. Studies have demonstrated substantial reductions in distortion through these compensation methodologies [13]. More sophisticated compensation methods further enhance accuracy by distinguishing

between systematic and random deviations, achieved through averaging data from multiple printed parts and applying smoothing techniques to filter out noise. Additionally, simulation-driven design extends to optimizing support structures, aiming to prevent cracking and minimize overall residual stress within the fabricated part [14, 15, 16, 17].

The current industry standard is to employ finite element (FE) simulation-based distortion predictions, using either calibrated inherent strains or thermomechanical simulations and using lumped or macro-layer approaches to approximate layer-by-layer buildup, to anticipate and compensate for the expected deformation. However, most FE-based simulation codes rely on voxel meshes that do not accurately represent complex part geometries, leading to poor stress and strain predictions in areas with intricate features. Additionally, many codes omit the plastic behavior of metals to reduce computation times. Achieving sufficiently fine voxel mesh to capture small features and stress risers within a practical time frame is challenging, causing inaccuracies in stress and strain predictions and limiting the applicability of ductile failure criteria that depend on plastic strains for predicting crack initiation.

Simulation method

We propose a method that combines a global simulation with one or more submodel simulations. The global simulation employs a voxel mesh and a thermomechanical and enhanced eigenstrain approach in a layer-by-layer manner, potentially using purely elastic material behavior to expedite computation. Details of the thermomechanical method and FE implementation can be found in [11] and [17]. From this global analysis, the resulting distortion field is mapped to the solid geometry's surface mesh (STL format), which is refined in regions experiencing higher distortion gradients, and certain structural features (e.g., topskin regions) can be selectively excluded from compensation to maintain aesthetic quality.

Submodel simulations then focus on high-strain regions, using a conformal hex mesh and the same layer-by-layer approach but with elastic-plastic material models and a triaxiality-dependent plastic strain-based ductile failure criterion to more accurately predict where cracks might initiate. These submodel FE meshes only represent smaller regions of higher strain, and a displacement boundary conditions from the global model are prescribed on submodel boundary, which allow these submodels to run quickly while providing precise local stress and strain results that inform improved support-structure designs.

Figure 1 shows the global and submodel simulation and shape compensation steps in the context of the overall workflow and data flow needed to generate toolpaths for printer from the nominal CAD model.

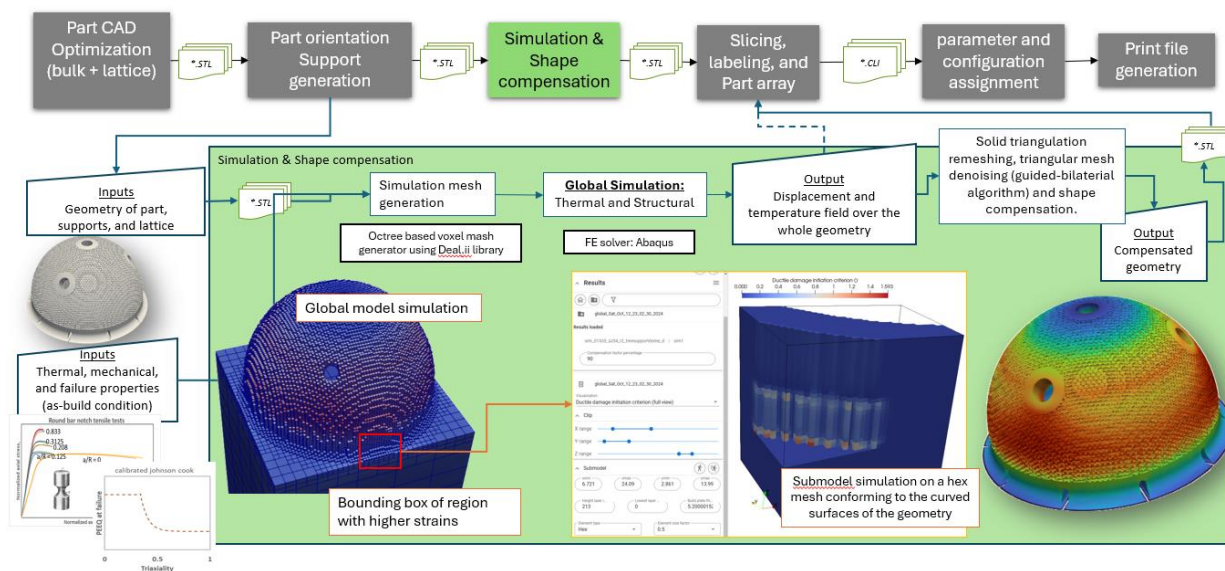


Figure 1: Simulation workflow

Iterative and measurement-based compensation improvements

Parts that experience large deformations often require iterative compensation. In each cycle, a distortion simulation uses the previously compensated geometry as input; adjustments continue until the change in predicted displacements falls below a chosen threshold. Figure 2 illustrates this workflow with a 1-D example.

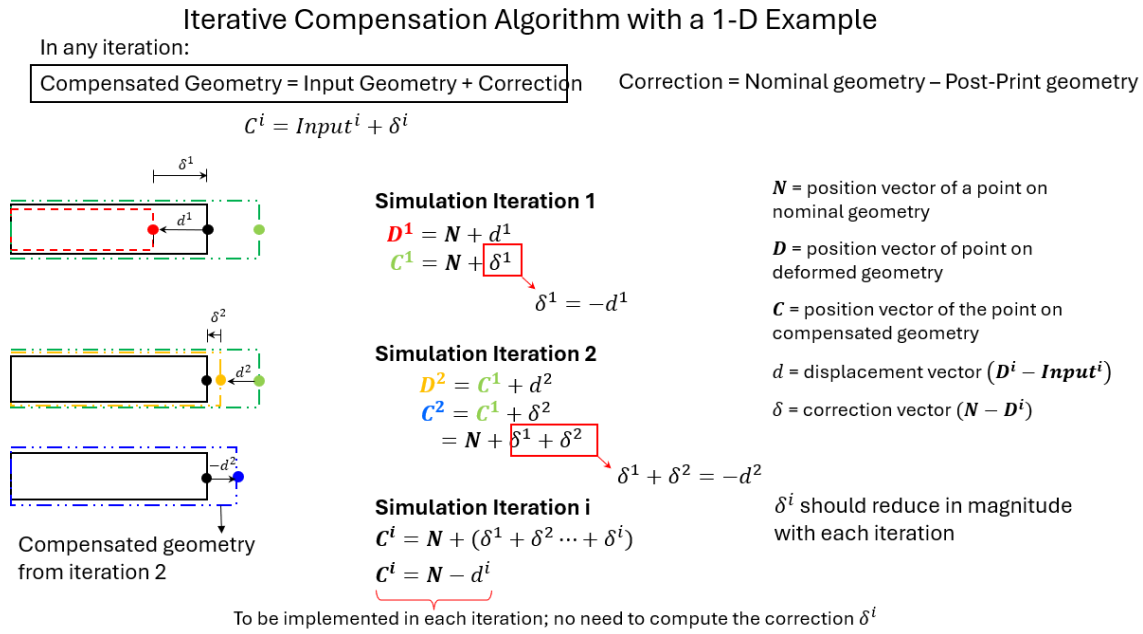


Figure 2: Algorithm for iterative compensation.

Because simulation accuracy is finite, an initially compensated part may still miss tight tolerances. We correct this in two steps. First, we print the compensated design and acquire high-resolution 3-D scans of the critical features; after denoising, deviations from several builds are averaged into an error field. Second, we overlay this field on the simulation-derived geometry to create a refined, more accurate compensation. The method parallels the earlier iterative loop, but substitutes experimental feedback for the second simulation (figure 3).

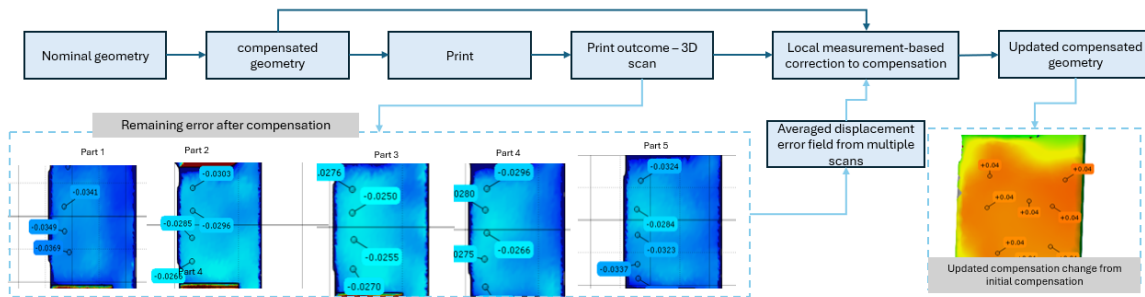


Figure 3: Measurement based correction to simulation compensation.

Material constitutive model calibration

We calibrated elastic-plastic material properties for Ti-6Al-4V (Ti64) by conducting tensile tests on as-printed vertical bars, and the triaxiality-dependent failure criteria parameters through testing additional bars with varying notch sizes. Figure 4 shows stress-strain response from tensile testing of as-printed Ti64 round cylindrical and notched bars and variation of plastic strain at failure against triaxiality.

We adopt a homogenized-material approach to idealize lattice regions in the global analysis. Homogenized properties for common lattice topologies are obtained with a representative-volume-element (RVE) method. A $3 \times 3 \times 3$ unit-cell RVE is built, then a uniaxial displacement field is applied under periodic boundary conditions on its bounding faces. The lattice struts inherit the bulk material parameters, and overall Young's modulus and yield strength are extracted from the volume-averaged stress-strain response. Figure 4 illustrates typical homogenized properties obtained from an RVE. We adopt a homogenized-material approach to idealize lattice regions in the global analysis. Homogenized properties for common lattice topologies are obtained with a representative-volume-element (RVE) method. A $3 \times 3 \times 3$ unit-cell RVE is built, then a uniaxial displacement field is applied under periodic boundary conditions on its bounding faces. The lattice struts inherit the bulk material parameters in the simulation of the RVE, and overall Young's modulus and yield strength are extracted from the volume-averaged stress-strain response.

For submodel simulations—driven by the global solution at the submodel boundary—we instead use a conformal tetrahedral finite-element mesh that resolves the lattice geometry explicitly and assigns the constituent material's properties directly, foregoing homogenization.

Figure 5 illustrates typical homogenized properties obtained from an RVE. Figure 6 shows that displacement fields generated by a FE simulation using the homogenized approach

compares well with those generated by a FE simulation that explicitly resolves the lattice geometry using a very fine FE mesh.

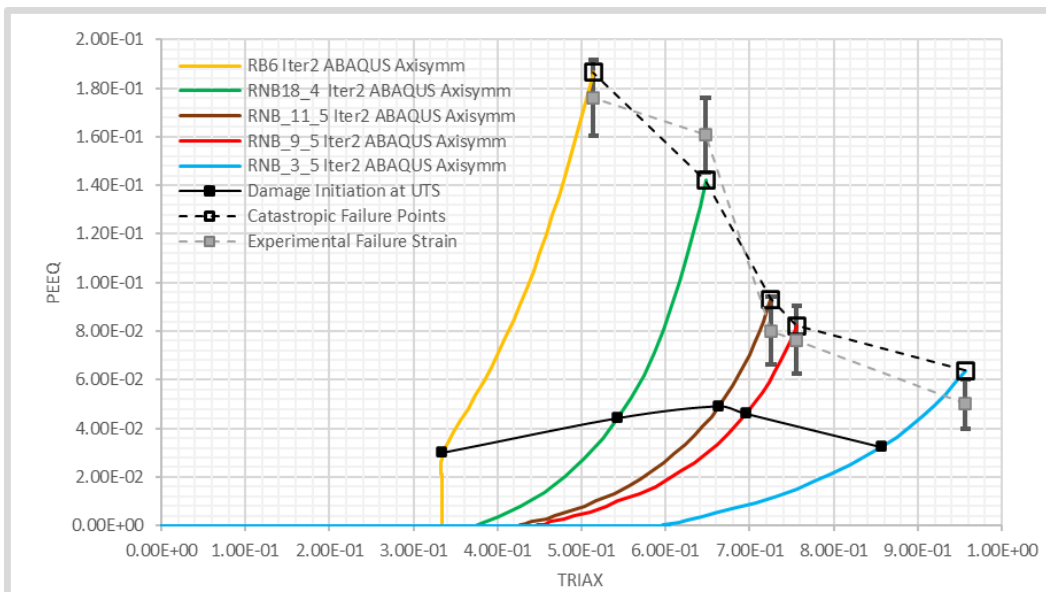
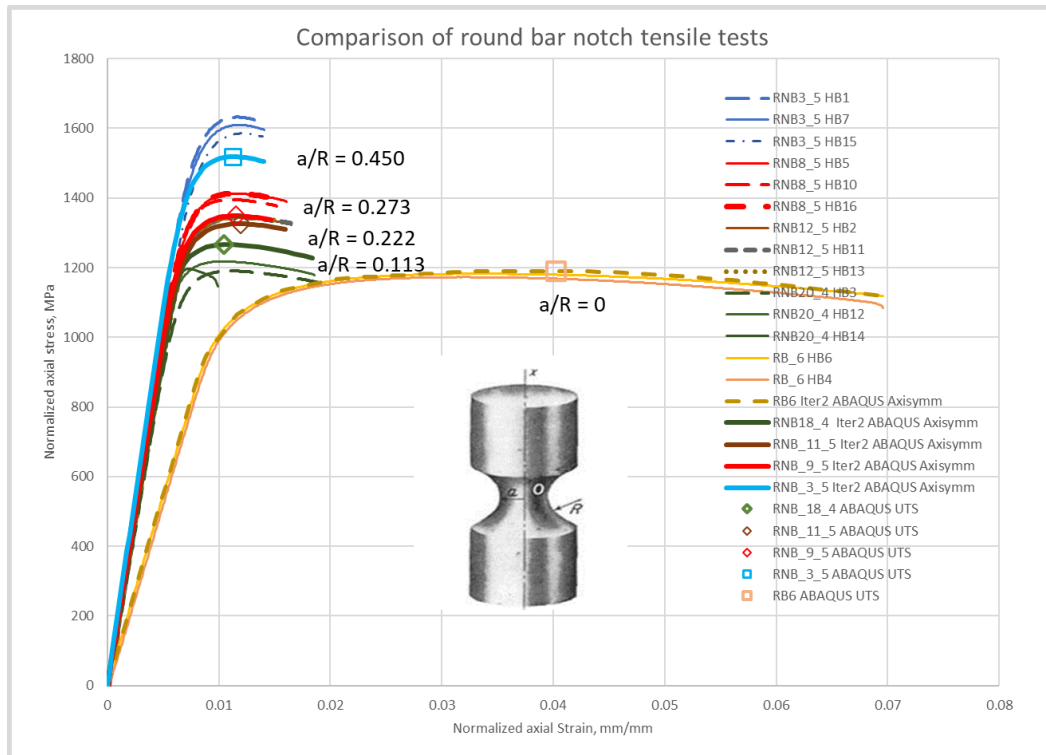


Figure 4: Triaxiality parameter based ductile failure criteria for as printed Ti64 bars.

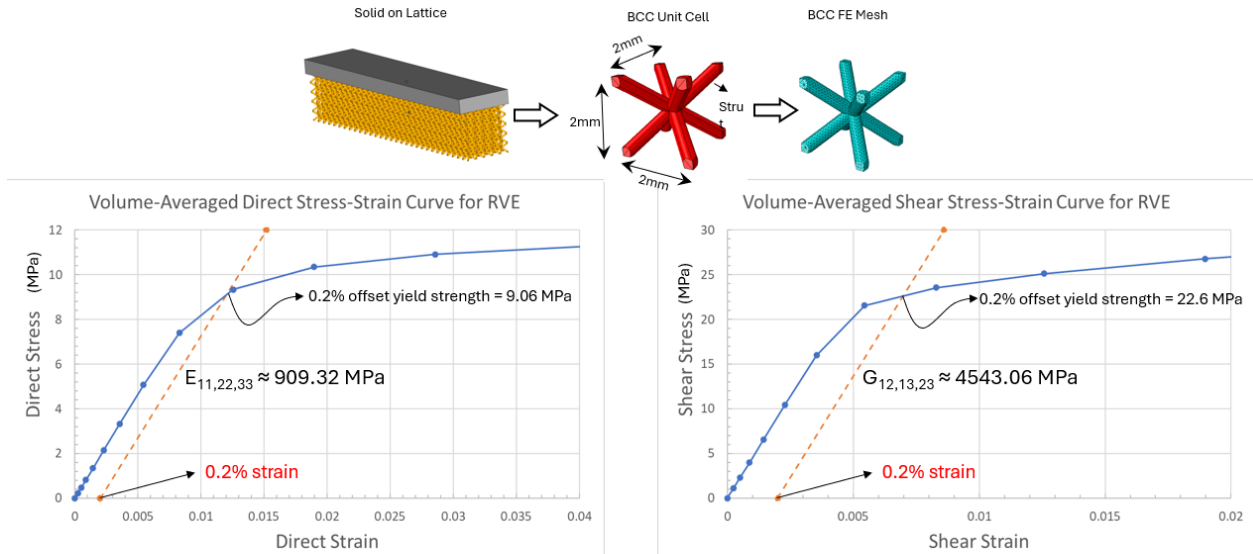


Figure 5: Homogenized properties for 2x2x2 BCC RVE constructed from Ti64.

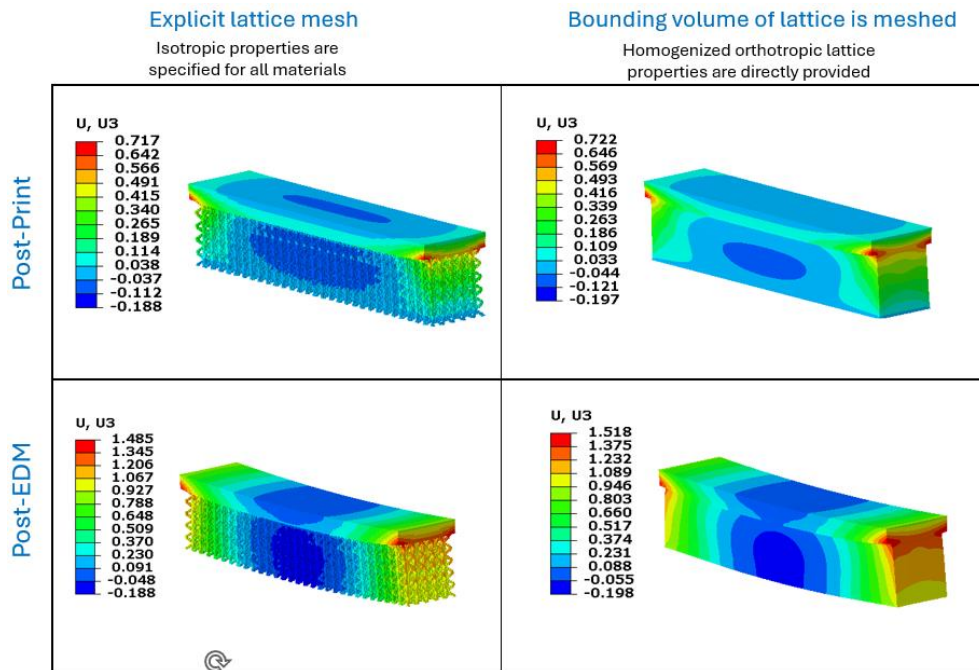


Figure 6: Comparison of displace field generated by the homogenized approach and a fine mesh FE simulation that explicitly resolves the lattice geometry.

Simulation and experimental results:

To validate the distortion prediction and compensation approach, parts of various geometries were fabricated, including specially designed specimens intended to fail under different triaxial stress states to demonstrate the accuracy of the failure predictions. A thermal camera (IR) was used to measure temperature distributions at the top of the layer providing data

to calibrate thermal boundary conditions. Furthermore, we compared thermal simulations that explicitly modeled the powder against those that did not, checking predicted layer temperatures against the IR measurements. If not otherwise mentioned below, simulations and experimental results are from parts fabricated using Ti64 powder on Ti64 plate. The size of the build plate is 600 mm x 600mm x 75 mm. We assume that the plate is held using kinematic couplings at three concentric points at the bottom of the plate. For thermal simulations, we apply a convective boundary condition on the top layer of the powder bed, on the bottom surface of the build plate, and side surfaces of the build plate. Initial temperature of the plate and the powder are kept at the room temperature. The side surfaces of the powder bed are assumed to be insulated. An example of FE mesh and structural boundary conditions are shown in Figure 7. Our simulations captured a range of distortion behaviors (e.g., warping and shrink-lines) and showed favorable agreement with experimental results in terms of overall part distortion, predicted failure, shape compensation, and layer temperature profiles.

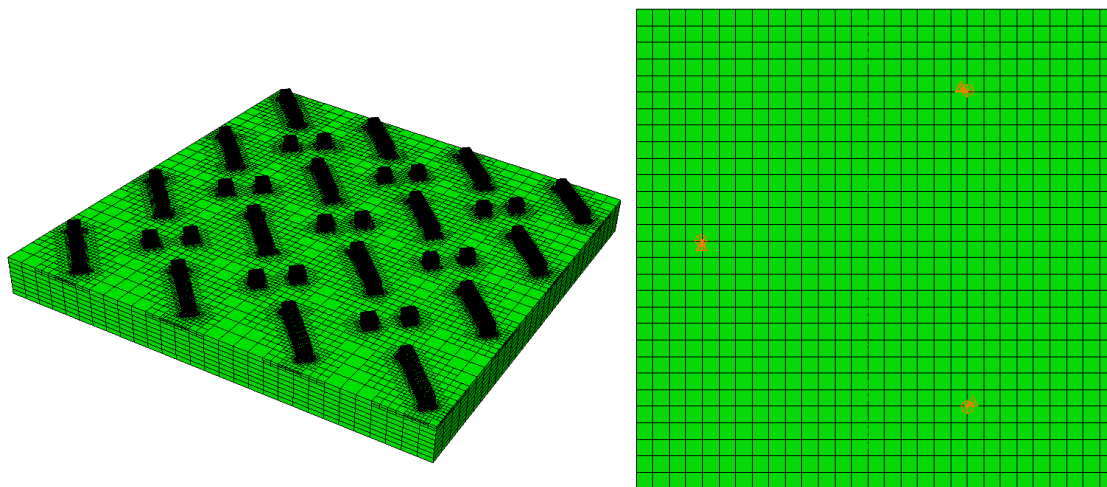


Figure 7: An example of the FE mesh and structural boundary condition at the bottom of the build plate.

Shape compensation

Figure 8 compares the dimensional deviation of a double-arch geometry printed with and without shape compensation. Dimensional measurements were made using a GOM scanner. Parts were printed and then separated from the build plate using EDM. After separation, parts experienced a spring-back deformation because of the residual stress that accumulated during the printing process because parts and the plate were not run through a vacuum stress relieving process. Simulation process predicted this spring back deformation in addition to the deformation during print. The compensated geometries were derived from the global simulation of the print and EDM steps. Forty parts were produced across several print runs and machines:

20 used compensated geometry, and 20 used nominal design. A statistical process-capability study confirms that the compensated parts achieved tighter dimensional tolerances.

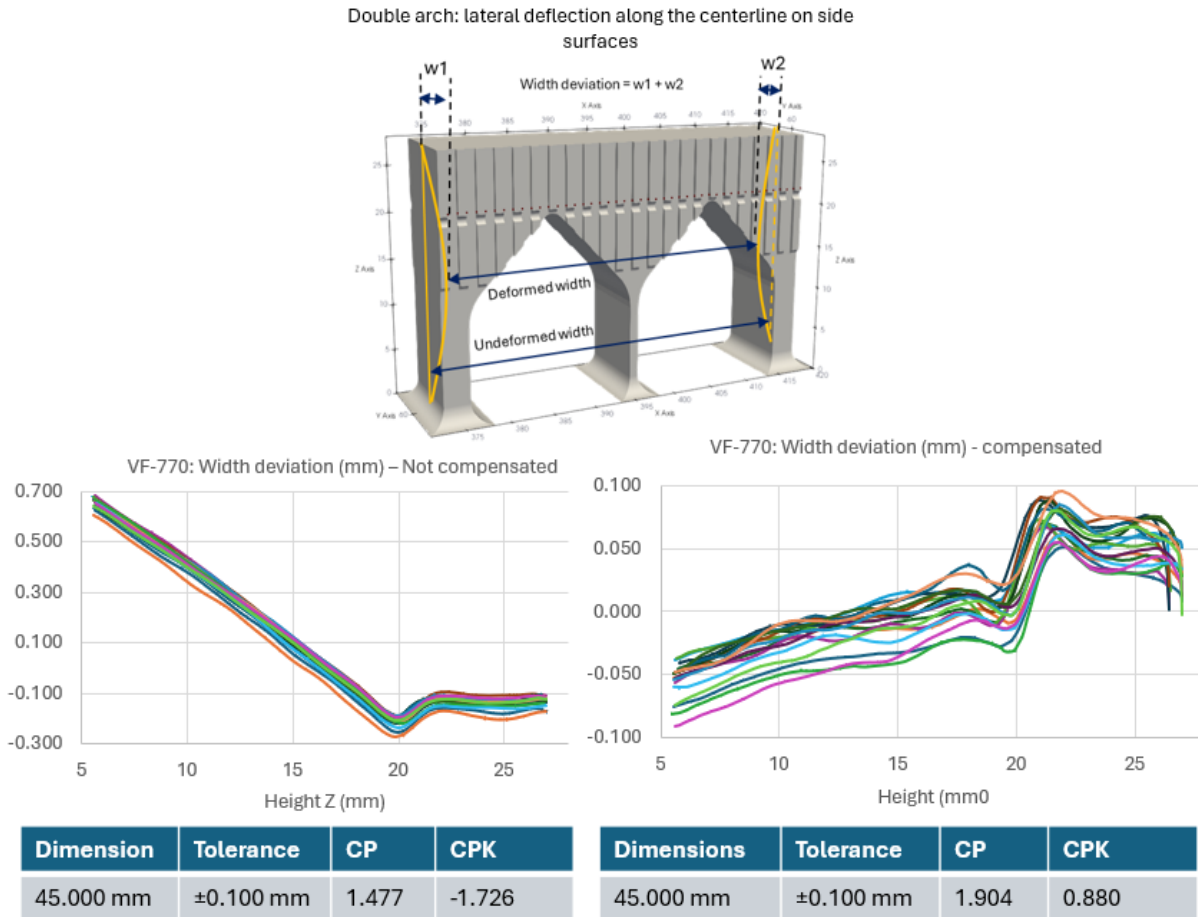


Figure 8: Dimensional improvement via simulation based compensation.

Part temperature prediction

Thermomechanical simulations employed a layer-averaged heat-input model in two variants. Case 1 (“no powder”) approximated heat loss to the surrounding powder with a convective boundary on the part’s sides. Case 2 (“powder”) added the powder bed to the domain, capturing conduction explicitly. Boundary conditions were calibrated by iteratively minimizing the gap between simulated temperatures and infrared-camera readings recorded after each layer. Calibration prints—horizontal/vertical bars, a double arch, and other simple shapes—produced a close match between prediction and measurement (Figure 9). Validation with a different layout and process settings (Figure 10) confirmed that including the powder bed improves accuracy: layer-average temperatures stayed within $\pm 5^\circ\text{C}$ of experimental values.

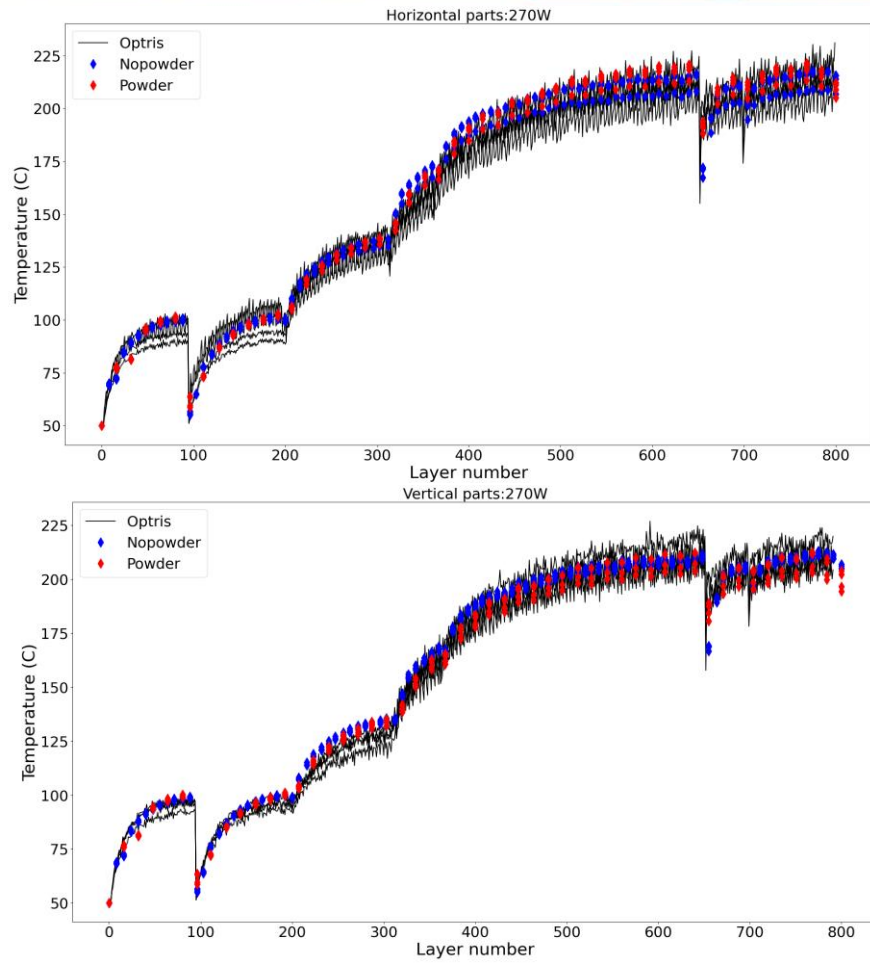
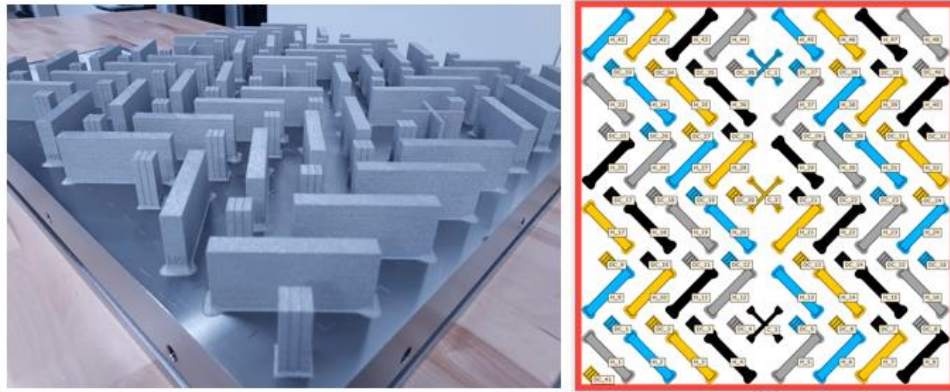
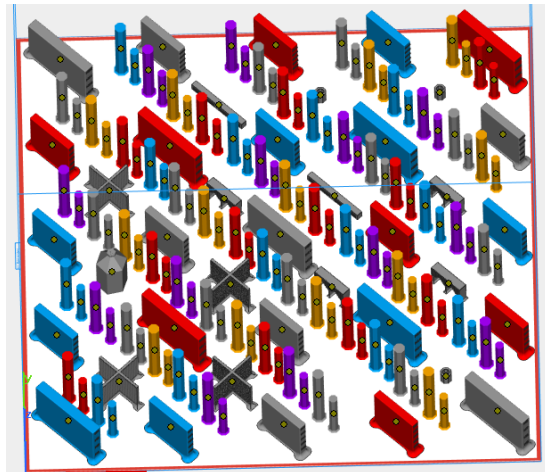


Figure 9: Print layout for thermal simulation's boundary condition calibration. Comparison of temperature generated from simulation and IR camera (Optris) measurement.



Vertical bar:305W

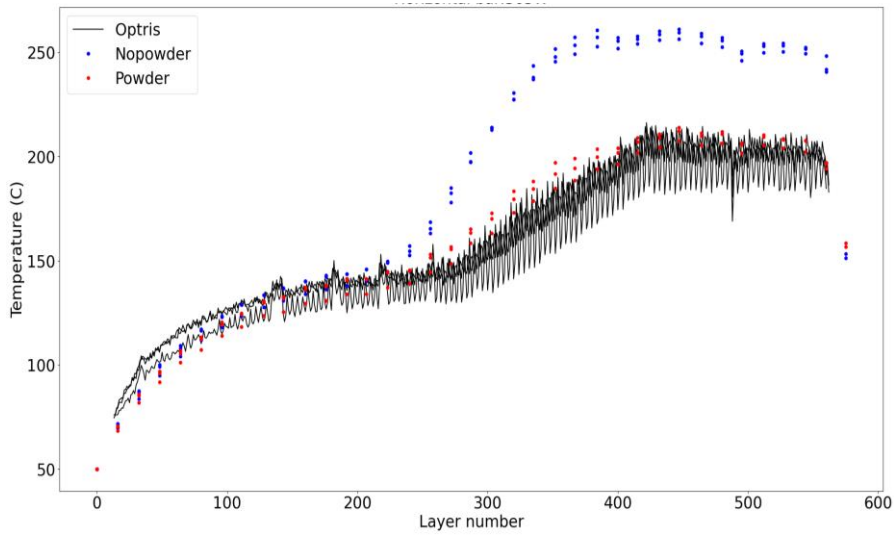
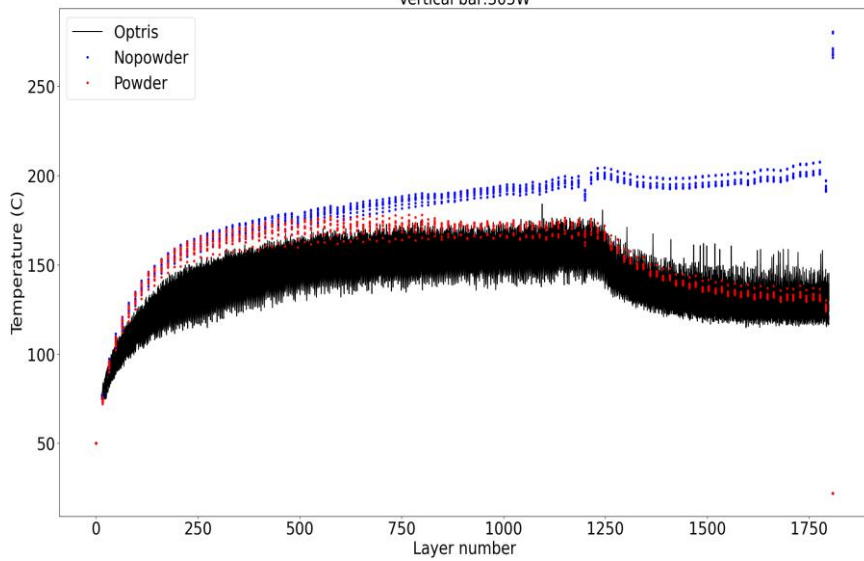


Figure 10: Print layout for the validation print. Comparison of temperature generated from simulation and IR camera (Optris) measurement.

Iterative and measurement-based compensation improvements

Figure 11 compares distortion predictions after three iterations for a highly distorted part.

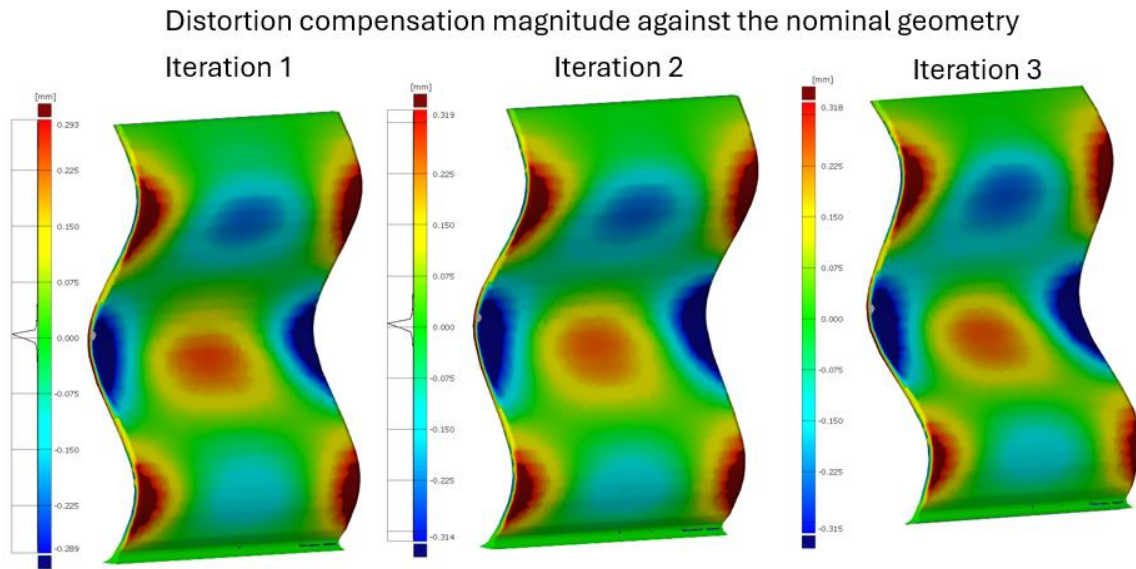


Figure 11: Distortions from an iterative compensation process.

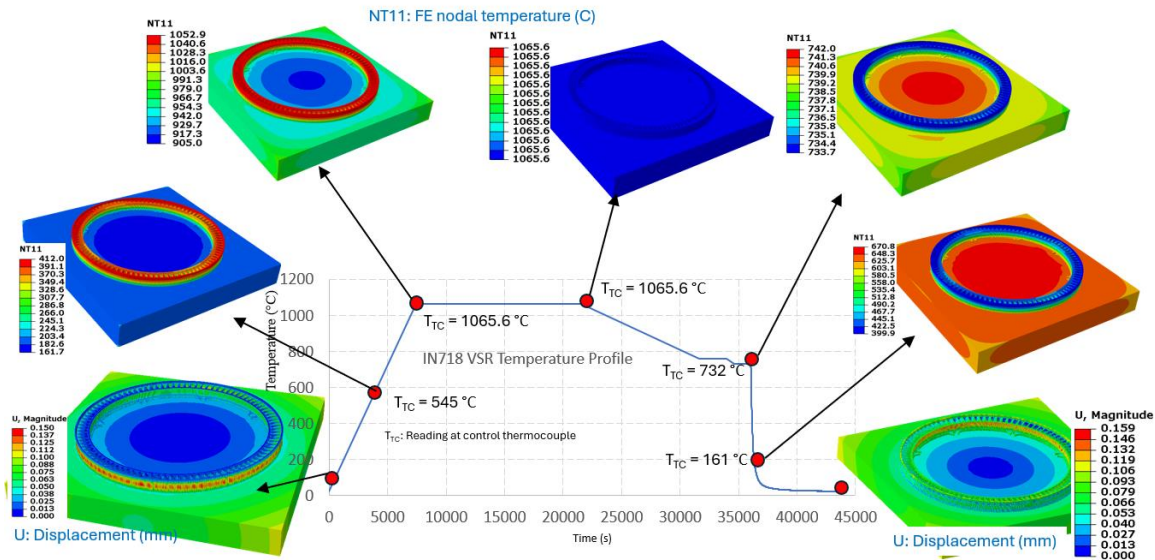


Figure 12: Thermomechanical simulation of the VSR process.

Part distortion during post print processing

A printed part can undergo further distortion during various post processing steps. We illustrate a scenario where a large circular part printed In718 on a steel plate (SS-304). Figure 12 shows results from a thermomechanical simulation of the VSR process. The build plate and the part are at the initial stress and deformation state of their as-printed condition. Figure 12 shows the as printed deformation state and the deformation state as the end of the VSR process, as well as temperature of the part and the plate at various stages of the process. The furnace heating on the part and the plate were simulated using radiation boundary condition on the outer surfaces. The deformation at the end and start of the VSR process is similar; but a residual stress is introduced in the part and the plate during the cooling phase of the VSR process due to the mismatch of the thermal expansion coefficient between In718 and SS304 steel. Due to this residual stress, the part undergoes a spring back deformation when it is separated from the plate via EDM. Figure 13 shows the deformation pattern of the part after EDM. This spring back deformation can be mitigated via a slower cooling to a temperature below 450 C. Final deformation was reduced by about 1 mm by using a slower cooling profile (see figure 14).

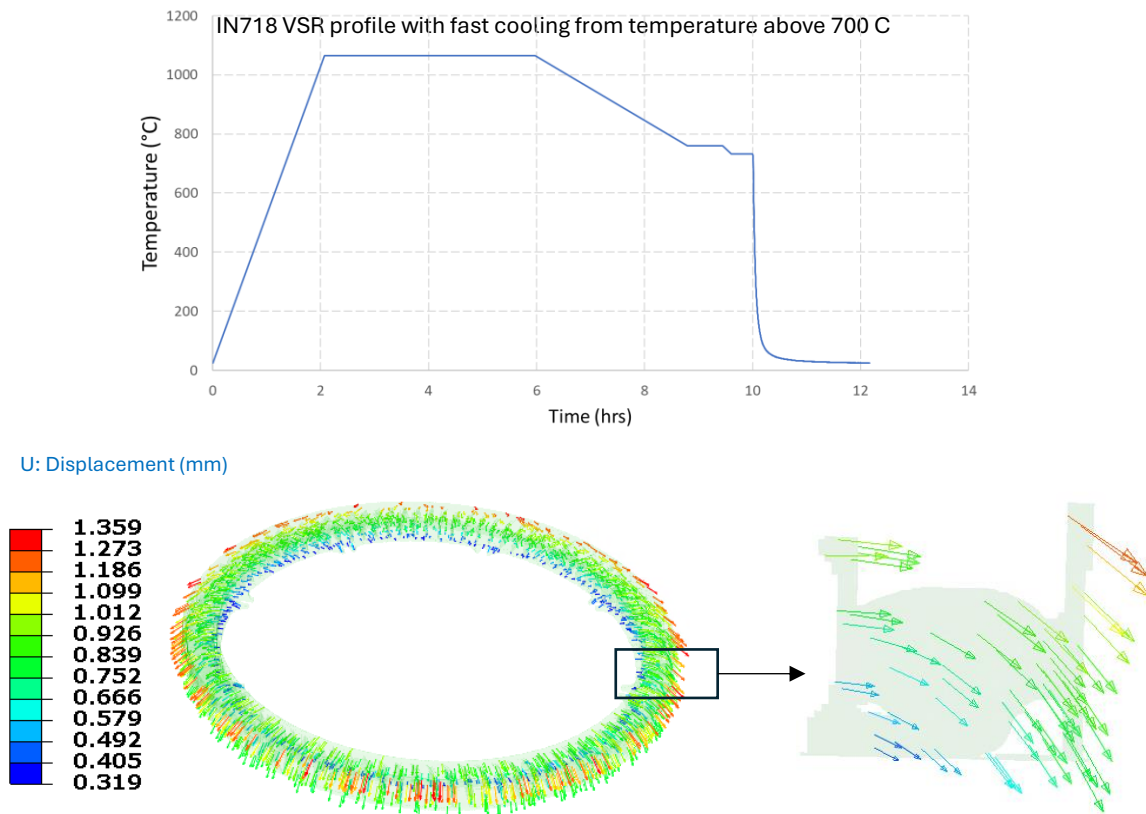
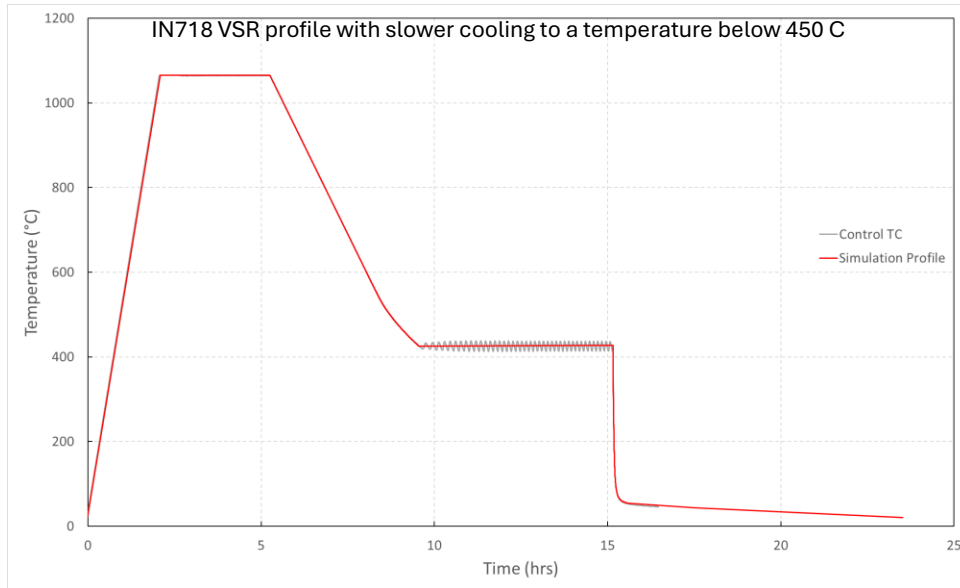
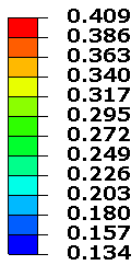


Figure 13: Temperature profile for VSR with fast cooling and deformation of the part after VSR and EDM operations showing a max deflection of 1.359 mm.



U: Displacement (mm)
U, Resultant



Difference in max.
displacements \approx 1 mm

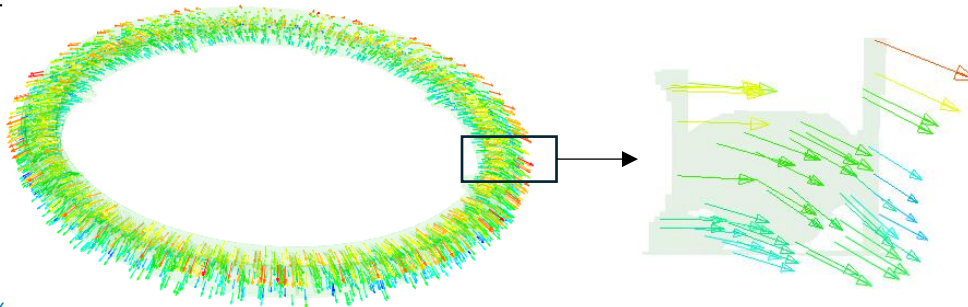


Figure 14: Temperature profile for VSR with slower cooling and deformation of the part after VSR and EDM operations showing a max deflection of 0.409 mm..

Build plate deformation:

We evaluate how build-plate deformation affects part dimensions by comparing two layouts (Figure 15). Layout 1 packs 3844 small parts at roughly 50 % fill, whereas Layout 2 prints 34 long bars at about 5 % fill. Temperature and corner-deflection trends diverge for these two cases (Figure 16): the dense layout heats rapidly with each layer, echoing its variable fill rate, while the sparse layout stabilizes thermally. In Layout 1 the plate expands chiefly in-plane, and that expansion bends the growing parts; the bending axis depends on each part's position (Figure 18). Most of this thermal expansion recovers during cooldown. By contrast, Layout 2 induces significant plate bending, lifting the corners so parts there finish slightly shorter in height. Layer-end temperature maps and deformation fields (Figure 17) confirm the picture:

higher energy input in the dense build drives transient expansion, whereas residual-stress-driven bending in the sparse build persists after cooling.

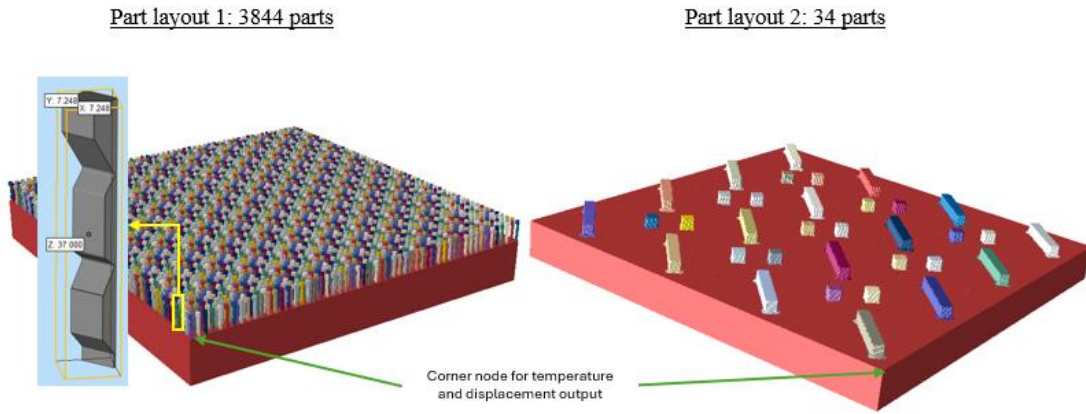


Figure 15: Two print layouts for study effect of plate deformation on parts' shape.

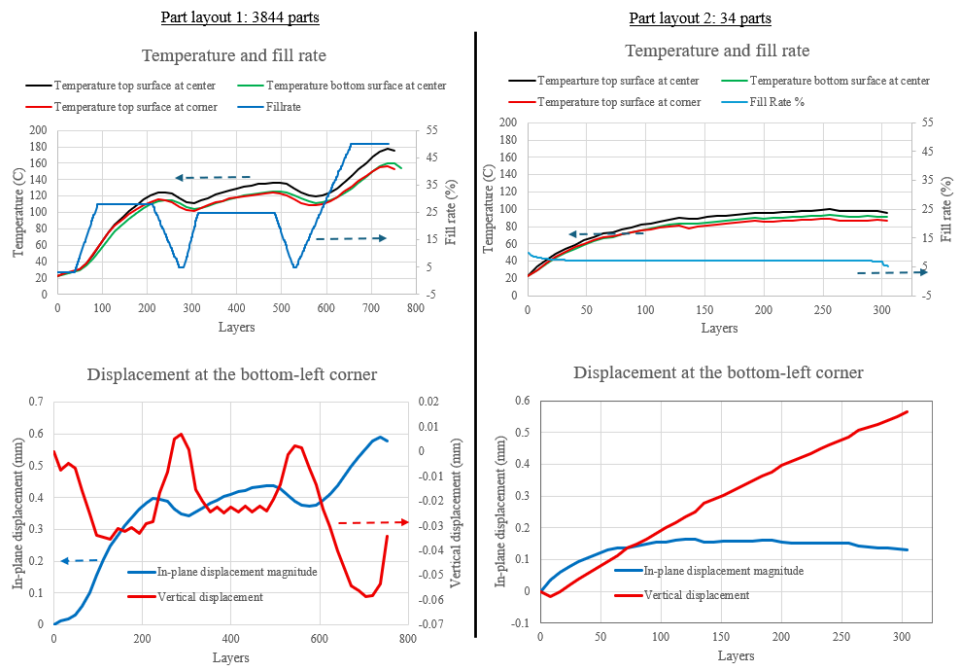


Figure 16: Temperature, and displacement of the build plate; and fill rates variations with layer for the two print layout for plate deformation study.

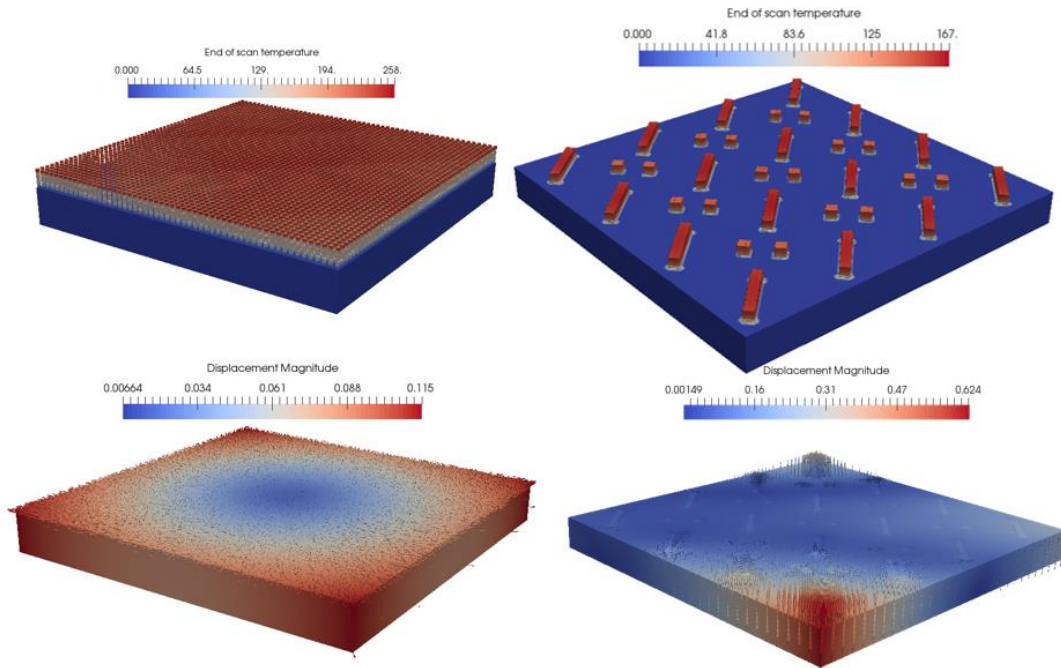


Figure 17: Temperature field at the end of scanning for each layer and displacement field of the part and the plate after cooling down at the end of print.

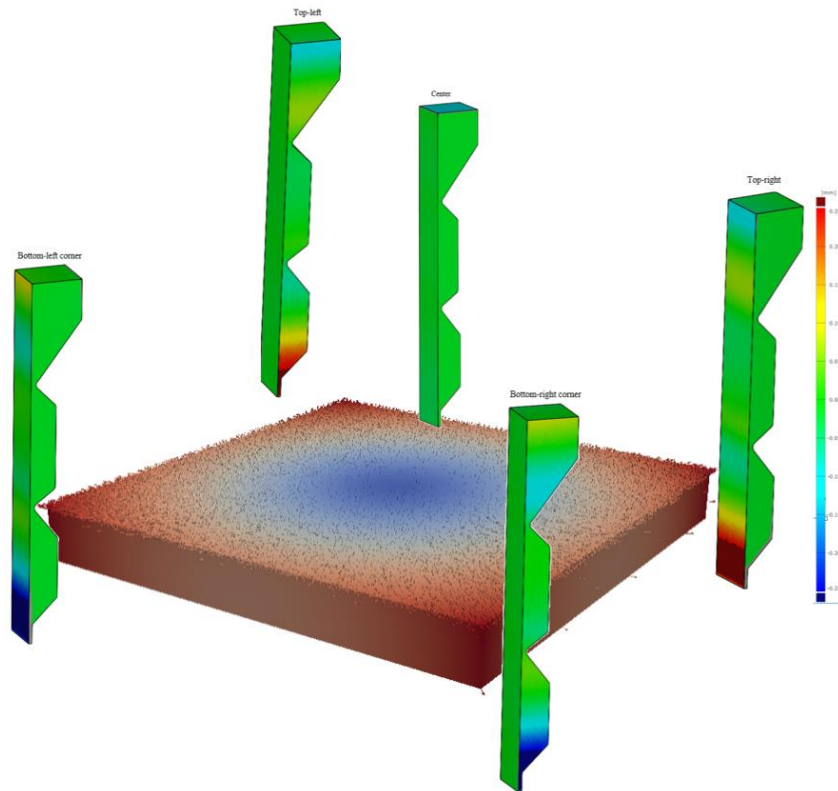


Figure 18: Surface deviation of parts printed at various location on the plate from layout 1. The part at the center of the plate shows least deformation. Parts from the corner show significant bending.

Failure criteria validation:

To verify the triaxiality-based ductile-failure criterion for Ti-6Al-4V (calibrated with round and notched bars), we created test parts whose geometries induce varied stress states in high-strain regions. Using the global-plus-submodel workflow, we predicted crack-initiation sites; Figure 19 maps these sites for each shape.

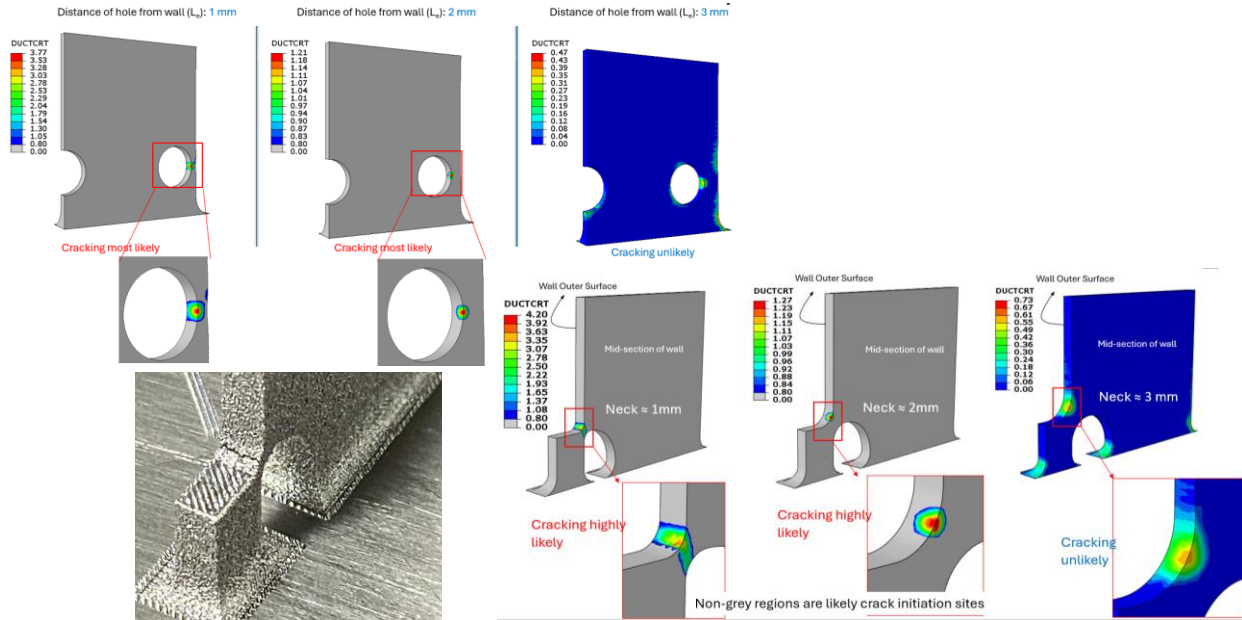


Figure 19: Various shapes and predicted crack initial sites. A value greater than 1 for the ductile damage criteria (DUCTCRT) indicates failure.

Limitations

This study has several limitations. While the enhanced inherent-strain (IS) framework that incorporates thermal history shows promise for simulation and shape compensation, its accuracy depends on calibration of IS values for specific materials and process windows; coupon-level calibrations may not generalize to complex geometries with varying wall thicknesses, supports, and fine features. The global voxel discretization can under-resolve thin walls, overhangs, and other local effects, and pre-calibrated IS values may not capture these phenomena. IS definitions become challenging for multi-material or functionally graded parts, and large distortions may violate the linear superposition often assumed by IS methods. Model fidelity is also sensitive to boundary-condition choices (e.g., build-plate attachment and support contacts), which are necessarily simplified. More broadly, the global model uses simplified physics (elastic behavior, layer-averaged heat input) and continuum treatments that omit microstructure and phase evolution; thermal boundary conditions were calibrated with IR data and may not transfer across machines, alloys, or process settings. Validation covered a limited set of parts and layouts, and post-processing was simplified, so residual-stress evolution may be incompletely represented. Consequently, although the enhanced IS approach is computationally efficient and valuable for early design guidance, practical dimensional accuracy often requires

hybrid workflows that combine simulation-based compensation with measurement-based corrections and, when needed, direct CAD offsets.

Conclusions

Our combined simulations and experiments confirm that the proposed workflow reliably predicts and mitigates distortion and failure in metal additive manufacturing. Layer-wise thermomechanical analyses—especially those that treat the surrounding powder as an explicit conductive domain—reproduce measured temperature profiles within ± 5 °C and capture key distortion modes such as warping, buckling, and shrink-lines. Failure sub-models, driven by global displacements, accurately localize crack nucleation under varied stress triaxialities, while simulation-derived shape compensation tightens dimensional tolerances across diverse geometries.

Iterative refinement further boosts accuracy: successive distortion runs or measurement-driven error-fields converge quickly, enabling large-deformation parts to meet stringent tolerances. Post-build studies show that residual stresses introduced during stress-relief cooling can trigger spring-back once the part is severed from the plate, but a slower cooling profile curbs final deformation by about 1 mm. Collectively, these results demonstrate that physics-based simulation, calibrated with targeted experiments and augmented by feedback loops, provides a robust foundation for first-time-right printing and informed post-processing.

Acknowledgements

The authors would like to acknowledge the contributions of former colleagues Ade Makinde, Ananad Amber, Daniel Wei, Saurabh Pui, Piotr Liebersbach, and Yuye Tang.

References:

1. Denlinger, E.R.; Michaleris P. Effect of stress relaxation on distortion in additive manufacturing process modeling. *Addit Manuf.* 2016;12:51–59. DOI:10.1016/j.addma.2016.06.011.
2. Denlinger, E.R.; Heigel JC; Michaleris P; Palmer TA. Effect of inter-layer dwell time on distortion and residual stress in additive manufacturing of titanium and nickel alloys. *J Mater Process Technol.* 2015;215:123–131. DOI:10.1016/j.jmatprotec.2014.07.030.
3. Denlinger, E.R.; Gouge M; Irwin J; Michaleris P. Thermomechanical model development and in situ experimental validation of the Laser Powder-Bed Fusion process. *Addit Manuf.* 2017;16:73–80.
4. Denlinger, E.R., Heigel, J.C., Michaleris, P., et al., Experimental validation of finite element modeling for laser powder bed fusion deformation, *Addit. Manuf.* 12 (2016) 108–120, <https://doi.org/10.1016/j.addma.2016.08.003>.

5. Chen, Q., X. Liang, D. Hayduke, J. Liu, L. Cheng, J. Oskin, R. Whitmore, A.C. To, An inherent strain based multiscale modeling framework for simulating part-scale residual deformation for direct metal laser sintering, *Addit. Manuf.* 28 (2019) 406–418.
6. Nachiket Patil, Rishi Ganeriwala, Jerome M. Solberg, Neil E. Hodge, Robert M. Ferencz; Benchmark multi-layer simulations for residual stresses and deformation in small additively manufactured metal parts, *Additive Manufacturing*, Vol 45, Sep 2021, 102015. <https://doi.org/10.1016/j.addma.2021.102015>.
7. Matthew Keller, Anil Bhaskar Chaudhary, Computational Process Model Development For Direct Digital Manufacturing: Powder Bed Processes; Final Report, AFRL-RX-WP-TR-2012-0516. Dec 2012.
8. Liang, X., L. Cheng, Q. Chen, Q. Yang, A.C. To, A modified method for estimating inherent strains from detailed process simulation for fast residual distortion prediction of single-walled structures fabricated by directed energy deposition, *Addit. Manuf.* 23 (2018) 471–486.
9. Liang, X., Chen, Q., Cheng, L., and To, A. (2017) A Modified Inherent Strain Method for Fast Prediction of Residual Deformation in Additive Manufacturing of Metal Parts. In: *Proceedings of Solid Freeform Fabrication (SFF) Conference*, 2017.
10. Liang, X., W. Dong, Q. Chen, S. Hinnebusch, Z. Zhou, A.C. To, A new procedure for implementing the modified inherent strain method with improved accuracy in predicting both residual stress and deformation for laser powder bed fusion, *Addit. Manuf.* 47 (2021) 102345.
11. Setien, Inaki, Michele Chiumenti, Maria San Sebastian, Carlos A. Moreira, and Manuel A. Caicedo. "Integrating temperature history into inherent strain methodology for improved distortion prediction in laser powder bed fusion." *Metals* 15, no. 2 (2025): 143.
12. H. Peng, M. Ghasri-Khouzani, S. Gong, R. Attardo, P. Ostiguy, B.A. Gatrell, J. Budzinski, C. Tomonto, J. Neidig, M.R. Shankar, R. Billo, D.B. Go, D. Hoelzle, Fast prediction of thermal distortion in metal powder bed fusion additive manufacturing: part 1, a thermal circuit network model, *Addit. Manuf.* 22 (2018) 852–868, <https://doi.org/10.1016/j.addma.2018.05.023>.
13. Lang Yuan and Pinghai Yang, From Art-to-Part: Multidisciplinary Virtual Toolset for Laser Power-bed Fusion Additive Manufacturing and Multi-Step Post Processing Certification; DMDII FINAL PROJECT REPORT. <https://apps.dtic.mil/sti/pdfs/AD1076873.pdf>
14. Cheng, L., X. Liang, J. Bai, Q. Chen, J. Lemon, A. To, On utilizing topology optimization to design support structure to prevent residual stress induced build failure in laser powder bed metal additive manufacturing, *Addit. Manuf.* 27 (2019) 290–304.
15. H. Peng, M. Ghasri-Khouzani, S. Gong, R. Attardo, P. Ostiguy, R.B. Rogge, B.A. Gatrell, J. Budzinski, C. Tomonto, J. Neidig, M.R. Shankar, R. Billo, D.B. Go, D. Hoelzle, Fast prediction of thermal distortion in metal powder bed fusion additive manufacturing: part

- 2, a quasi-static thermo-mechanical model, *Addit. Manuf.* 22 (2018) 869–882, <https://doi.org/10.1016/j.addma.2018.05.001>.
16. Moustapha Jadayel and Farbod Khameneifar, Improving Geometric Accuracy of 3D Printed Parts Using 3D Metrology Feedback and Mesh Morphing; *J. Manuf. Mater. Process.* 2020, 4, 112; doi:10.3390/jmmp4040112
17. Setien, I., Chiumenti, M., van der Veen, S., San Sebastian, M., Garciandía, F. and Echeverría, A., 2019. Empirical methodology to determine inherent strains in additive manufacturing. *Computers & Mathematics with Applications*, 78(7), pp.2282-2295., <https://doi.org/10.1016/j.camwa.2018.05.015>.